Spin–orbit coupling in the L-gap surface states of Au(111): spin-resolved photoemission experiments and first-principles calculations

J Henk[1]**, M Hoesch**[2,3]**, J Osterwalder**[2]**, A Ernst**[1] **and P Bruno**[1]

[1] Max-Planck-Institut für Mikrostrukturphysik, Weinberg 2, D-06120 Halle, Saale, Germany
[2] Physik-Institut, Universität Zürich, Winterthurerstrasse 190, CH-8057 Zürich, Switzerland
[3] Swiss Light Source, Paul-Scherrer-Institut, CH-5232 Villigen PSI, Switzerland

E-mail: henk@mpi-halle.de

Abstract
The spin–orbit-split L-gap surface states on Au(111) are investigated by means of spin- and angle-resolved photoelectron spectroscopy and relativistic first-principles calculations, the latter including both electronic structure and photoemission. The dispersion, momentum distribution and spin polarization of the surface states are consistent with those of a two-dimensional electron gas with Rashba–Bychkov spin–orbit coupling (SOC). The surface symmetry manifests itself in the spin-integrated photoemission intensities, thereby providing details of the orbital composition of the surface states. For the spin polarization, modulations which show up in theory are below the experimental detection limit of 5%. The dependence of both dispersion and spin polarization on the SOC strength are addressed theoretically. The combination of experiment and theory establishes a consistent picture of the L-gap surface states.

(Some figures in this article are in colour only in the electronic version)

1. Introduction

Spin–orbit-split electronic states are commonly realized by a two-dimensional electron gas (2DEG) in a semiconductor heterojunction. The structural asymmetry at the interface between the two semiconductors gives rise to the Rashba–Bychkov interaction [1, 2] which leads to both splitting and spin polarization of these free-electron-like states. Detailed investigations of the electronic structure were performed mainly by means of de Haas–van Alphen oscillations and by optical methods which are—compared to spin- and angle-resolved photoelectron spectroscopy—rather indirect spectroscopies.

Recently, it turned out that the Shockley surface states on the (111) surfaces of noble metals are paradigmatic realizations of spin–orbit-split electronic states, too [3, 4]. Located at a metal surface, these can be easily accessed by angle-resolved photoelectron spectroscopy, providing information on the dispersion and on the strength of the spin–orbit interaction [5, 6]. In particular for Au(111), spin–orbit coupling is strong enough for detecting the splitting even in spin-integrated photoelectron spectroscopy. The spin polarization of the L-gap surface states was first predicted by theory [6, 7] and later investigated experimentally [8, 9]. These studies focused mainly on the basic properties, such as the experimental demonstration of spin-polarized emission and the observation of the spin structure in reciprocal space. The purpose of the present paper is to explore details of the surface states by means of a joint experimental and theoretical investigation. We combine spin- and angle-resolved photoemission experiments, relativistic first-principles calculations and—based on the latter—photoemission calculations that form a direct link between the experimental spectra and the *ab initio* results.

The L-gap surface states can be simply described as free electrons, providing a connection to a two-dimensional electron gas. Looking more closely, however, deviations from the behaviour of an isotropic 2DEG show up [10], which are related to the symmetry of the Au(111) surface. The threefold rotational symmetry manifests itself in an azimuthal modulation of the spin polarization and of the photoemission intensity. A second effect is brought about by the corrugation of the surface potential which results in a small but non-zero spin-polarization component normal to the surface. The question arises of whether these effects which showed up in recent theoretical calculations [11] appear also in the present experiment, in particular in spin-resolved Fermi surface mapping [12].

Spin-integrated photoemission spectra in off-normal emission show a distinct intensity relation upon reversal of the detection azimuth. This 'linear dichroism' can be explained analytically on the basis of the orbital composition of the surface states which results from the surface symmetry and from spin–orbit coupling, supported by first-principles calculations.

To reach a conclusion from the experimental spin polarization of the photoelectron on that of the L-gap surface states could—in principle—be difficult because the photoemission process itself produces spin-polarized electrons even from non-spin-polarized initial states, an effect of the spin–orbit interaction [13]. Therefore, one needs to link the photoemission experiments (i.e., the excited states) with *ab initio* calculations for the initial states. This connection is provided by photoemission calculations within the relativistic one-step model. The theoretical spectra depend sensitively on some of the free parameters which could be fixed by comparison of a few theoretical spectra with their experimental counterparts. The overall agreement of experimental and theoretical spectra establishes thus a consistent picture of the anatomy of the L-gap surface states.

The paper is organized as follows. Spin–orbit coupling at a metal surface is sketched in section 2, with mathematical details being provided in the appendix. Experimental and theoretical aspects are discussed in sections 3 and 4. Section 5 comprises the discussion of selected results. First, it focuses on spin-integrated data, namely on the dispersion and momentum distribution (section 5.1) and on 'linear dichroism' (section 5.2). The spin polarization is addressed for normal emission (section 5.3) and for angular scans in constant-initial-energy mode (section 5.4). Finally, the effect of spin–orbit coupling on the surface states is discussed theoretically (section 5.5).

2. Spin–orbit coupling at a metal surface

Spin–orbit coupling (SOC) at a metal surface with free-electron-like surface states shows a close analogy to that in a two-dimensional electron gas, as was established recently for the

(111) surfaces of noble metals [7, 14]. The main ideas and results will be briefly repeated in the following.

Spin–orbit coupling is strong where the crystal potential changes rapidly. This is in particular the case for heavy atoms—such as Au—close to the atomic nucleus. A second contribution is attributed to the presence of the surface. The latter breaks the symmetry of the bulk system, for example the inversion symmetry or the mirror symmetry with respect to the surface-parallel layers. Hence, the surface potential barrier can be regarded as a structural asymmetry which results in additional SOC, in analogy to the Rashba–Bychkov effect in 2DEGs [2] and the Dresselhaus effect in bulk systems without inversion symmetry [15]. To be more specific: a 2DEG is confined to the interface between two different semiconductors (say, GaAs and GaAlAs). A free-electron-like surface state at the (111) surface of a noble metal is asymmetrically confined to the surface region: towards the interior of the solid by the bulk band gap, towards the vacuum by the surface barrier. The strength of the 'atomic' SOC exceeds that of the surface contribution, as was argued by Mugarza *et al* [16].

The free-electron nature of the surface states lends support to a description in terms of plane waves (see the appendix), with the advantage that the atomic contribution to the SOC need not be considered explicitly. In a 2DEG with Rashba–Bychkov SOC, Kramers' degeneracy is lifted and the eigenstates are split in energy,

$$E_\pm(\boldsymbol{k}_\parallel) = \tfrac{1}{2}\boldsymbol{k}_\parallel^2 \pm \gamma |\boldsymbol{k}_\parallel|, \tag{1}$$

with $\boldsymbol{k}_\parallel = (k_x, k_y)$. The momentum distribution consists of two concentric circles separated by $\approx 2\gamma$. The quantity γ reflects the strength of the structural asymmetry which for Au(111) is 3–5 times larger than in typical semiconductor 2DEGs [14]. Its sign determines which state is the 'inner' one ('+' for $\gamma > 0$, '−' for $\gamma < 0$) and which is the 'outer' one ('−' for $\gamma > 0$, '+' for $\gamma < 0$).

Associated with the above splitting is a complete spin polarization $\boldsymbol{P}_\pm$ of the electronic states which is within the xy-plane and perpendicular to the in-plane wavevector $\boldsymbol{k}_\parallel = |\boldsymbol{k}_\parallel|(\cos\varphi_e, \sin\varphi_e)$,

$$P_\pm^x(\boldsymbol{k}_\parallel) = \alpha_\pm \sin\varphi_e, \qquad P_\pm^y(\boldsymbol{k}_\parallel) = -\alpha_\pm \cos\varphi_e, \qquad P_\pm^z(\boldsymbol{k}_\parallel) = 0, \tag{2}$$

with $\alpha_\pm = \mp 1$ (compare (A.7)). For the discussion, it is advantageous to decompose $\boldsymbol{P}_\pm$ into radial and tangential components,

$$P_\pm^{\mathrm{rad}} = P_\pm^x \cos\varphi_e + P_\pm^y \sin\varphi_e, \qquad P_\pm^{\mathrm{tan}} = P_\pm^x \sin\varphi_e - P_\pm^y \cos\varphi_e. \tag{3}$$

The spin polarization of the + (−) surface state rotates anticlockwise (clockwise) about the z-axis, that is, $P_\pm^{\mathrm{rad}} = 0$ and $P_\pm^{\mathrm{tan}} = \mp 1$. By measuring $P_\pm^{\mathrm{tan}}$ for the two surface states, the inner surface state can be associated either with the + or with the − state and analogously for the outer surface state. By this means, one can reach a conclusion as regards the sign of γ which is *a priori* not known.

For Au(111), the x- and y-axes of the coordinate system were chosen along the crystallographic [1$\bar{1}$0] and [$\bar{1}\bar{1}$2] directions, respectively, with the z-axis pointing along the surface normal (towards the vacuum). Hence, the yz-plane is a mirror plane of the crystal (figure 1). In reciprocal space, the k_x-axis is along the $\overline{\mathrm{K}}$–$\overline{\Gamma}$–$\overline{\mathrm{K}}$ direction of the two-dimensional Brillouin zone (2BZ), whereas the k_y-axis is along $\overline{\mathrm{M}}$–$\overline{\Gamma}$–$\overline{\mathrm{M}}$.

The Au(111) surface shows a threefold rotational symmetry which allows in principle for a non-zero $P_\pm^z$ as well as for a deviation from the circular momentum distribution. It turned out that the latter is negligible, suggesting expanding $\boldsymbol{P}_\pm$ in terms of φ_e. The leading terms of $P_\pm^x$ and $P_\pm^y$ remain as in (2), but $P_\pm^z$ turns into

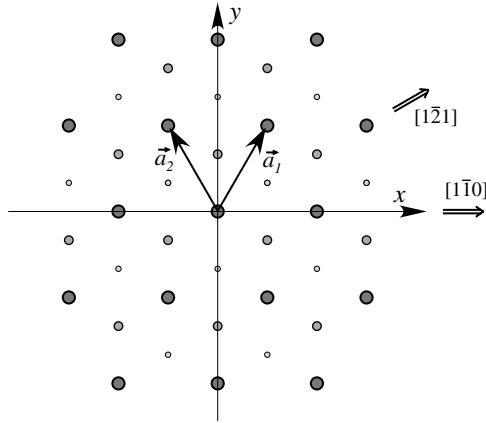$$P_\pm^z(\boldsymbol{k}_\parallel) = \beta_\pm \cos 3\varphi_e. \tag{4}$$

Figure 1. The atomic arrangement of the Au(111) surface, represented by the three outermost layers (large dots: first layer; medium-sized: second layer; small: third layer). The basis vectors a_1 and a_2 span the hexagonal layer lattice. The $[1\bar{2}1]$ ($\bar{\Gamma}$–$\bar{M}$ in reciprocal space) and $[1\bar{1}0]$ ($\bar{\Gamma}$–$\bar{K}$) crystallographic directions are indicated.

The presence of a non-zero $P_{\pm}^{z}$ requires non-vanishing in-plane components of the potential gradient (compare (A.1)). Thus, $P_{\pm}^{z}$ is brought about by the surface corrugation, i.e., the in-plane asymmetry of the surface potential and, hence, is expected to be small ($|\beta_{\pm}| \ll 1$). A non-zero $P_{\pm}^{z}$ is accompanied by a non-complete in-plane spin polarization ($|\alpha_{\pm}| < 1$).

The mirror yz-plane of the system forces the spin polarization $P_{\pm}$ of the L-gap surface states along x for $\varphi_e = 90°$ ((2) and (4)). Note that the system remains non-magnetic since time-reversal symmetry dictates $P_{\pm}(k_{\parallel}) = -P_{\pm}(-k_{\parallel})$.

3. Experimental aspects

Spin-integrated and spin-resolved photoelectron spectroscopy measurements were performed using the photoemission instrument COPHEE [12] at the surface and interface spectroscopy beamline (SIS) at the Swiss synchrotron light source. COPHEE, the COmplete PHotoEmission Experiment is equipped with a three-dimensional polarimeter. The sample is mounted on a two-axis goniometer, in order to allow performance of angle-scanned experiments. For all results presented in this paper, the light source was set to a photon energy of $h\nu = 21.1$ eV with linear p polarization. The angle between the photon incidence and the emission directions was kept fixed at $\alpha = 45°$ (figure 2).

The sample was cleaned by many repeated cycles of Ar-ion bombardment and annealing. During the experiments it was cooled to approximately 150 K. The sample quality remained unchanged over at least half a day, as judged from the photoemission linewidth of the surface states at normal emission. An account of the experimental spectra is given in [8] and the measured spin structure is discussed in [9].

To be more specific, the schematic set-up of the experiment is shown in figure 2. The sample can be rotated about the polar rotation axis in the surface plane and the azimuthal axis normal to the surface. Two Mott detectors (MDs) are mounted in such a way that both of them can measure the longitudinal polarization component P_{MD}^{z} along the photoemission direction. The other sensitive axes P_{MD}^{x} and P_{MD}^{y} of each MD are inclined at $\pm 45°$ with respect to the polar rotation axis. To measure the surface-state electrons, the sample was rotated by small
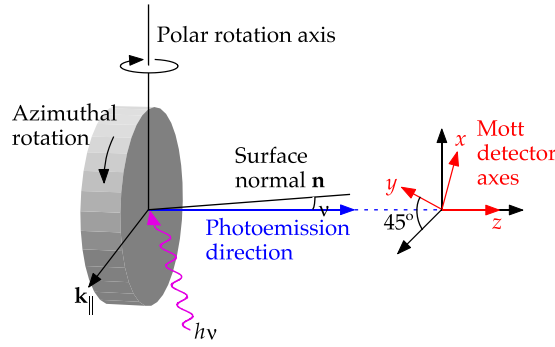
Figure 2. The set-up of the photoemission experiment. The sample (grey) can be rotated about two axes. The surface normal n lies within the scattering plane, the latter spanned by the light incidence direction and the detection direction (indicated in addition by $k_\parallel$). The local coordinate system of the Mott detector (MD (red)) comprises the z-axis along the detection direction and the x- and y-axes which are at 45° with respect to the polar rotation axis.

polar angles of up to $\theta = 7°$ and, thus, P^z_{MD} corresponds well to the out-of-plane polarization component (along the surface normal), while P^{tan} and P^{rad} are measured as 45° projections onto the P^x_{MD}- and P^y_{MD}-axes. All spin-resolved data were acquired using just one of the Mott detectors and the direction of the spin-polarization vector was cross-checked for a sufficiently large number of scans with the other detector. The 45° projection was taken into account for the analysis of the in-plane polarization component ($P^{tan} = \sqrt{2}\, P^y_{MD}$).

Conventional spin-integrated photoemission spectra and Fermi surface maps were taken using the channeltron detector mounted in a standard geometry in the hemispherical electron analyser. The resolution of the spectrometer was better than 20 meV in energy and 0.5° FWHM in angle for these data sets. Spin-resolved data were acquired both as energy distribution and as angular distribution scans, the latter translating into curves for $k_\parallel$ momentum distribution. In both cases, the energy and angular resolutions of the spectrometer were relaxed to 120 meV and 1.8° FWHM, respectively.

The measurement of spin-resolved spectra from a non-magnetic sample imposes two specific requirements on the data analysis.

 (i) The lack of a macroscopically defined magnetization direction—as is present in a magnetic sample—implies that a natural and unique spin-quantization axis for *all* measurement geometries is missing. Instead, the spin-quantization axis depends on the azimuth of electron motion, as given by $k_\parallel$ (section 2). In the rotating-sample geometry of the COPHEE experiment, the tangential (P^{tan}) and the normal (P^z) spin-polarization components are naturally projected onto the sensitive axes of the MDs.

(ii) In a conventional experiment on a magnetic sample, a systematic offset of the spin-resolved intensities—due to the residual intrinsic detection asymmetry of the MDs—can be cancelled out by reversing the magnetization direction. This procedure, however, cannot be carried out in the case of a non-magnetic sample because there is no net magnetization to reverse. It is thus necessary to deduce the instrumental detection asymmetry from the data themselves, relying on very fundamental assumptions (e.g., time-reversal symmetry). For Au(111), an angular scan across the normal-emission direction which covers both positive and negative polar angles ϑ_e is equivalent to reversing the spin of the initial states (if the theoretical model in section 2 is correct). To get rid of the asymmetry, the sensitivity of one of the detector channels in each detector pair in the polarimeter is adjusted until a

well-balanced result was obtained for a complete data set, including angular scans across the surface normal [8]. This procedure is *a posteriori* corroborated by comparison with the theoretical photoemission intensities.

The error margin of the spin-polarization measurements is dominated by the statistical error of counting the electrons in the detectors. An additional systematic uncertainty is imposed by the procedure for removing the instrumental detector asymmetry. The total detection limit for the spin polarization at intensity maxima is approximately $\Delta P = \pm 5\%$ (degree of polarization).

The in-plane wavevector $\boldsymbol{k}_\parallel$ is determined by the kinetic energy E_{kin} of the photoelectrons and the detection angles ϑ_e and φ_e, the latter taken with respect to the z-axis (surface normal) and the x-axis (figure 1),

$$\boldsymbol{k}_\parallel = \sqrt{2E_{\text{kin}}} \begin{pmatrix} \cos \varphi_e \\ \sin \varphi_e \end{pmatrix} \sin \vartheta_e. \tag{5}$$

4. Theoretical aspects

4.1. Ab initio calculations

The electronic structure of Au(111) was computed within the local spin-density approximation (LSDA) to density-functional theory (DFT), using the Perdew–Wang exchange–correlation potential [17]. The electronic structure of the 1×1 surface was calculated self-consistently by the Korringa–Kohn–Rostoker (KKR) method, with the muffin-tin potentials of the six outermost surface layers and of the three adjacent vacuum layers (with so-called empty muffin-tin spheres) allowed to differ from the bulk potential. A comparison of the potential of the sixth surface layer with that of the bulk showed no significant difference, implying that the surface region is sufficiently large for a correct description of the surface states.

The potential in the vacuum region required particular attention. Using the fcc parent lattice of the bulk also in the vacuum layers resulted in too low a binding energy of the L-gap surface states, indicating too steep a surface barrier. While there is no reason which forces one to use the parent lattice in vacuum (because of the missing ionic core potentials), the interlayer distance for the vacuum layers in the self-consistent calculations was deliberately increased. An increase by 4% with respect to the bulk interlayer distance resulted in good agreement with the experimentally obtained surface-state binding energies (0.51 eV compared to 0.49 eV [6] at $\overline{\Gamma}$). This relaxation is further corroborated by the work function, which is too high for the fcc case (5.97 eV) but agrees nicely for the relaxed case (5.23 eV) with experimental data (5.31 eV [18]).

The Au(111) surface shows a $22 \times \sqrt{3}$ reconstruction (the so-called herringbone reconstruction [19, 20]), which mainly leads to surface *umklapp* processes and, hence, affects slightly the photoemission intensities [21]. Since Fourier transform scanning tunnelling spectroscopy showed no effect of the reconstruction and reveals the L-gap surface states of the 1×1 unit cell, the latter was exclusively considered in theory.

The effect of SOC on the electronic structure was addressed by interpolating between the relativistic (Dirac equation) and the scalar-relativistic case [22, 23]. This allowed us to manipulate SOC while keeping the other relativistic effects, a method which is superior to the usual scaling of the speed of light c. Even a 'super-relativistic' case could be investigated, by artificially enhancing the SOC (section 5.5).

The electron density at the surface is significantly changed with respect to that in the bulk. In particular, its gradient can be become considerable. Therefore, the LSDA might be not

sufficient and gradient corrections—such as the generalized gradient approximation (GGA)—might be in order. However, it turned out that the GGA is not without problems [24]. Although the GGA gives in general good total energies, it leads to an unphysical charge accumulation close to a classical turning point of the potential. The surface barrier imposes such a classical turning point and, thus, a LSDA exchange–correlation potential [17] was used in the present investigation.

4.2. Photoemission calculations

Besides the electronic structure, spin- and angle-resolved photoemission intensities were calculated within the relativistic one-step model, formulated in a layer KKR manner [25, 26]. The possibility of directly comparing experimental and theoretical results is of particular importance for systems with strong SOC. Since SOC can lead to spin-polarized photocurrents even from non-spin-polarized initial states [13], one should be aware that the spin polarization of photoelectrons excited from a spin-polarized L-gap surface state could differ from that of the respective initial state. In this context, it appears worth noting that the photoemission calculations rely on the same *ab initio* potentials as the electronic structure calculations for the ground-state properties (section 4.1) and take into account SOC via the Dirac equation.

The *ab initio* calculations provide the ground-state properties of the system, whereas photoemission deals with an excited system. The associated many-body effects could be accounted for by the self-energy Σ. The latter can in principle be obtained from first principles, e.g., within the GW approximation [27], but these computations are very demanding—especially for surfaces—and are beyond the scope of the present paper. Instead, one typically approximates Σ by an energy-dependent but homogeneous optical potential $V_{opt}(E)$ which is added to the energy E. The real part of V_{opt} shifts the energies of the electronic states; its imaginary part accounts for the finite lifetimes of the quasi-particles, i.e., for both the photohole ($E < E_F$) and the photoelectron ($E > E_F$). In contrast to the case in a previous publication [14], the actual values of V_{opt} could now be determined by comparing theoretical with experimental spectra. Here, the focus lay in particular on the intensity relations of the 'inner' and the 'outer' surface state for opposite detection azimuths φ_e. This allowed a unique determination of V_{opt} for the photoelectrons. It turned out that just in the experimental kinetic energy range (around 16 eV for 21.1 eV photon energy), several comparably flat bands exist in the unoccupied band structure, beside a free-electron-like band. These are shifted in energy by $Re(V_{opt})$ and affect the final state of photoemission (i.e., the time-reversed LEED state), therefore explaining the strong dependence of the theoretical intensities on the optical potential. For 21.1 eV photon energy, $V_{opt} = (0 - 0.06i)$ eV and $V_{opt} = (-1.5 - 2.4i)$ eV were taken for the initial states (photoholes) and for the final states (photoelectrons), respectively.

Other free parameters in the photoemission calculations were fixed by convergence tests (see [26] for details on layer KKR and photoemission approaches). For example, 30 atomic layers contributed to the photocurrent, the maximum angular momentum in the expansion of the scattering solutions was $l_{max} = 4$ and the number of plane waves in the interlayer scattering was about 60.

The electric field $\mathbf{A}$ of the incident light was treated within the framework of Fresnel's theory. Thus, taking $\mathbf{A}$ constant inside the solid, in particular at the surface, gradient corrections to the photoemission matrix elements are neglected [25]. To support this procedure we note that Fresnel's theory proved to be successful in describing experimental photoemission from Fe(110) [28]. Second, going beyond Fresnel's theory did not significantly improve theoretical spectra for metal surfaces [29].

4.3. Definitions of spin polarization

In the discussion of various aspects of spin polarization, attention has to be directed briefly to its definition [30, 31]. The spin polarization P_N of the initial states is defined in terms of the spin-resolved spectral density $N(E, \boldsymbol{k}_\parallel)$, namely

$$P_N(E, \boldsymbol{k}_\parallel) = \frac{N_\uparrow(E, \boldsymbol{k}_\parallel) - N_\downarrow(E, \boldsymbol{k}_\parallel)}{N_\uparrow(E, \boldsymbol{k}_\parallel) + N_\downarrow(E, \boldsymbol{k}_\parallel)}, \tag{6}$$

where the spin orientations $\uparrow$ and $\downarrow$ refer to a chosen spin-quantization axis (compare section 2). This is an intrinsic spin polarization which is independent of any measurement and can be calculated from first principles. The spin polarization P_I of the photoelectrons, however, relies on the particular set-up which is used in the experiment (e.g., detection direction, light incidence direction and polarization, photon energy). It is defined by the spin-resolved photocurrent $I(E_{\text{kin}}, \boldsymbol{k}_\parallel)$ obtained for this specific set-up,

$$P_I(E_{\text{kin}}, \boldsymbol{k}_\parallel) = \frac{I_\uparrow(E_{\text{kin}}, \boldsymbol{k}_\parallel) - I_\downarrow(E_{\text{kin}}, \boldsymbol{k}_\parallel)}{I_\uparrow(E_{\text{kin}}, \boldsymbol{k}_\parallel) + I_\downarrow(E_{\text{kin}}, \boldsymbol{k}_\parallel)}. \tag{7}$$

It is *prima vista* not obvious how closely P_N and P_I are connected. Their relation is provided by photoemission theory, in particular by numerical photoemission calculations. Sometimes we do not explicitly distinguish between P_N and P_I because it should be clear from the context what definition is meant.

5. Discussion and results

In the following, our experimental and theoretical results are presented. After the discussion of the dispersion of the L-gap surface states (section 5.1), their intensity variation with polar angle of detection is addressed (section 5.2). Subsequently, the focus lies on the spin polarization, in particular for normal emission (section 5.3) and for off-normal emission (section 5.4). The effects of SOC strength and of the surface potential corrugation are addressed theoretically in section 5.5.

5.1. Dispersion and momentum distribution

A first check of whether the free-electron model and the first-principles calculations describe the experiment appropriately is provided by the comparison of the dispersion relations $E_\pm(\boldsymbol{k})$ and of the momentum distributions. Inspection of figure 3 shows that the L-gap surface states do indeed behave almost like free electrons with Rashba–Bychkov spin–orbit interaction. In both the experimental dispersion and the momentum distribution (figures 3(c) and (d)) obtained from the spin-integrated measurements, the splitting in energy and in $\boldsymbol{k}_\parallel$ is clearly seen.

Parabolic fits to the peak positions in the experimental energy distribution curves and in the theoretical spectral densities gave binding energies of 0.47 eV (experiment) and 0.51 eV (theory) at $\boldsymbol{k}_\parallel = 0$. An effective mass of $m^\star = 0.25\,m_e$ in experiment indicates that the dispersion is too strong in theory, the latter showing $m^\star = 0.20\,m_e$. This is also evident from the Fermi wavenumbers k_F which read 0.160 and 0.186 Å^{-1} in experiment (figures 3(c) and (d)) and 0.149 and 0.172 Å^{-1} in theory (figures 3(a) and (b)).

The SOC strength γ shows up as a splitting $\Delta k_\parallel$ (compare (1)). The experimental $\Delta k_\parallel$ of 0.026 Å^{-1} agrees well with 0.023 Å^{-1} from theory. The former corresponds to $\gamma = 396$ meV Å, which is about 3–5 times larger than for 2DEGs in semiconductor heterojunctions [14].
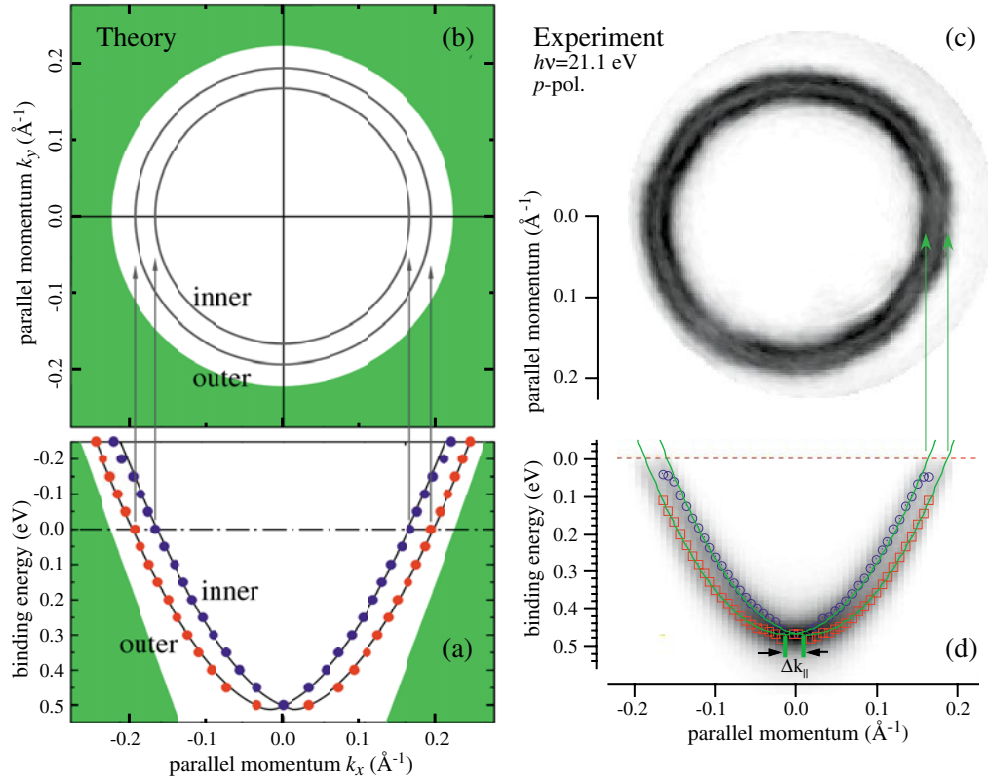
Figure 3. Spin–orbit splitting of the L-gap surfaces states on Au(111). (a) The dispersion along k_x of the inner (black (blue) circles) and the outer (grey (red) circles) surface state, as obtained from the first-principles calculations. The region of bulk bands is shaded in grey (green). (b) The theoretical momentum distribution of the surface states at the Fermi energy E_F. (c) The experimental Fermi surface map, as obtained from the spin-integrated photoemission intensities. (d) The experimental dispersion map in an arbitrary azimuth. The peak positions as determined from peak fitting to the energy distribution curves are indicated by circles (red and blue) and parabolic fits to these positions are shown by solid lines (green). In both experimental panels, the measured intensity is shown on a linear scale, with black corresponding to the largest intensity.

5.2. Variation of the photoemission intensity with the polar angle of emission

Considering solely the dispersion does not provide detailed information on the surface-state wavefunctions. The latter can be probed by analysing the angular dependence of the photoemission intensities, an approach which already proved to be successful in determining the orbital composition of the dangling-bond surface state on GaAs(110) [32].

The angular dependence of the spin-integrated intensities is exemplified for three polar angles of emission: $\vartheta = 0°$ (normal emission, $\mathbf{k}_\parallel = 0$) and $\pm 3.6°$ (off-normal emission at $|\mathbf{k}_\parallel| = \pm 0.135$ Å^{-1}). For $\vartheta = 0°$, the measured surface states are degenerate ($E_{\text{outer}}(0) = E_{\text{inner}}(0)$) and produce the sharp maximum at 0.47 eV binding energy (solid in figure 4(b)). For off-normal emission, this peak is split into two maxima with significantly less intensity: the outer surface state shows a binding energy of about 0.22 eV, the inner, one of about 0.12 eV ($E_{\text{outer}}(\mathbf{k}_\parallel) < E_{\text{inner}}(\mathbf{k}_\parallel)$). The most striking fact, however, is the intensity variation at the peak positions upon reversal of ϑ. The intensity I_{outer} of the outer surface state increases when turning $\vartheta = -3.6°$ (dashed (purple) in figure 4(b)) to $+3.6°$ (solid (green)),
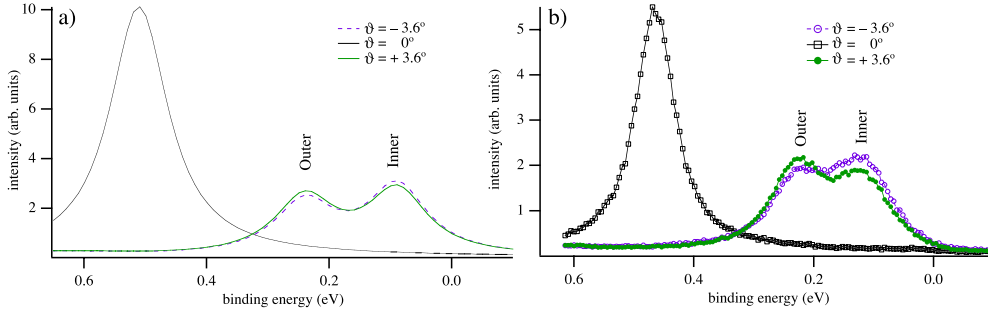
Figure 4. Spin-integrated intensities for different polar angles of detection (as indicated) in the $\varphi = 75°$ azimuth (compare figure 1). (a) Theoretical energy distribution curves. (b) Measured spectra from the data set shown in figure 3.

whereas the intensity I_{inner} of the inner one shows the opposite behaviour. Note further that the intensity differences are of about the same amount, ΔI. With the definitions $\boldsymbol{k} = (+\boldsymbol{k}_\parallel, k_\perp)$ and $\tilde{\boldsymbol{k}} = (-\boldsymbol{k}_\parallel, k_\perp)$, the experimental intensity relations can be simply cast as $I_{\text{outer}}(\boldsymbol{k}) = I_{\text{inner}}(\tilde{\boldsymbol{k}}) = \overline{I} + \Delta I$ and $I_{\text{outer}}(\tilde{\boldsymbol{k}}) = I_{\text{inner}}(\boldsymbol{k}) = \overline{I} - \Delta I$ (we note in passing that these relations hold also for other $\boldsymbol{k}_\parallel$). The theoretical photoemission intensities (figure 4(a)) agree reasonably well with the experimental ones, with differences being attributed to the surface-state dispersion and the SOC strength γ. The question arises of how these similarities and differences in behaviour can be explained.

At $\boldsymbol{k}_\parallel = 0$, the surface states belong to the Λ_6 representation of the double group C$_{3v}$ (in Schoenflies notation [33]), with the spatial part of the wavefunction belonging to the Λ^1 single-group representation. Thus, the surface states consist mainly of s, p$_z$ and d$_{z^2}$ orbitals, with relative spectral weights of 8.2%, 76.0% and 8.9%, respectively (as obtained from the first-principles calculations). Note that these orbitals are even under mirror operations of the surface. At $\boldsymbol{k}_\parallel \neq 0$ in an azimuth which lies not within a mirror plane of the surface (here: $\varphi_e = 75°$; compare figure 1), the wavefunctions achieve additional contributions from p orbitals oriented within the surface plane. For the polar angles in figure 4 these have relative spectral weights of up to about 23%.

Expressing the surface-state wavefunctions as $|e\rangle \pm |o\rangle$ (with energy E_i) and taking a single plane wave $|\boldsymbol{k}\rangle$ (with energy E_f) as the final state, the photoemission intensity $I(\boldsymbol{k})$ is given by Fermi's golden rule,

$$I_\pm(\boldsymbol{k}) \propto |\langle \boldsymbol{k}|\boldsymbol{A} \cdot \boldsymbol{\nabla}|e\rangle \pm \langle \boldsymbol{k}|\boldsymbol{A} \cdot \boldsymbol{\nabla}|o\rangle|^2 \, \delta(h\nu - E_f - E_i). \tag{8}$$

Here, $\boldsymbol{A}$ is the electric field vector of the incident light. Simple manipulation yields $I_\pm(\boldsymbol{k}) = \overline{I}(\boldsymbol{k}) \pm \Delta I(\boldsymbol{k})$, with

$$\overline{I}(\boldsymbol{k}) \propto |\boldsymbol{A} \cdot \boldsymbol{k}|^2 \left(|\langle \boldsymbol{k}|e\rangle|^2 + |\langle \boldsymbol{k}|o\rangle|^2 \right) \delta(h\nu - E_f - E_i), \tag{9a}$$

$$\Delta I(\boldsymbol{k}) \propto 2|\boldsymbol{A} \cdot \boldsymbol{k}|^2 \, \text{Re}(\langle \boldsymbol{k}|e\rangle\langle o|\boldsymbol{k}\rangle)\delta(h\nu - E_f - E_i). \tag{9b}$$

The even part $|e\rangle$ of the surface-state wavefunction comprises mainly s and p$_z$ orbitals and, hence, obeys $\langle \boldsymbol{k}|e\rangle = \langle \tilde{\boldsymbol{k}}|e\rangle$. The odd part $|o\rangle$, however, contains mainly p orbitals oriented along $\boldsymbol{k}_\parallel$ and shows $\langle \boldsymbol{k}|o\rangle = -\langle \tilde{\boldsymbol{k}}|o\rangle$. This establishes $\overline{I}(\tilde{\boldsymbol{k}}) = \overline{I}(\boldsymbol{k})$ and $\Delta I(\tilde{\boldsymbol{k}}) = -\Delta I(\boldsymbol{k})$, which yield immediately $I_\pm(\tilde{\boldsymbol{k}}) = I_\mp(\boldsymbol{k})$ (note that $\boldsymbol{A} \cdot \boldsymbol{k}$ is constant in the present experimental set-up (figure 2)).

Associating the inner and the outer surface-state wavefunctions with $|e\rangle \pm |o\rangle$, respectively, the intensity variation observed in figure 4 can be related to the interference term $\Delta I(\boldsymbol{k})$.
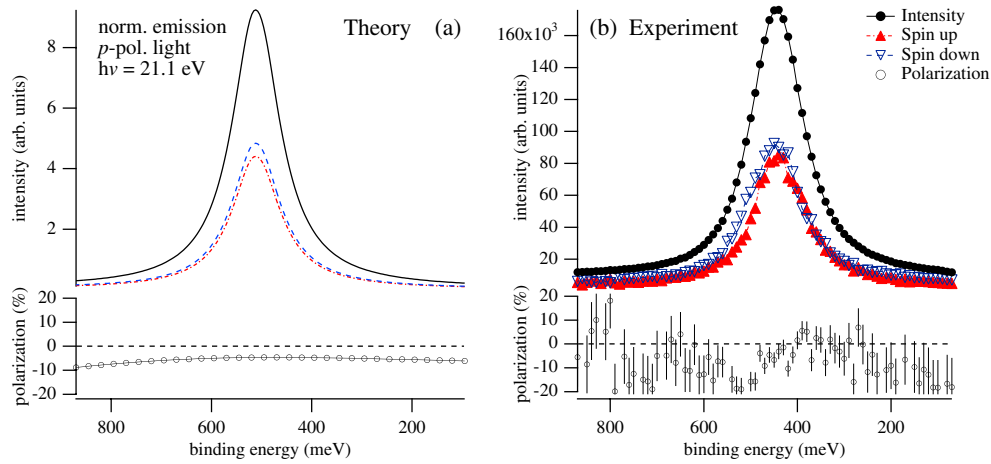
Figure 5. Spin-resolved normal photoemission from the L-gap surface states. (a) Theoretical intensities are obtained for p-polarized light incident within the yz-plane ($\overline{\Gamma}$–$\overline{M}$ azimuth) and 21.1 eV photon energy. The total intensity (solid, black) is decomposed into spin up (dashed, blue) and spin down (dashed-dotted, red), with the spin-quantization axis along x. (b) The experimental spectrum at normal emission. The spin polarization is calculated from the P^{rad} component of the Mott detector.

Without this term, the two surface states would have the same intensity $\overline{I}(k)$ at a given $k_{\parallel}$, as is the case to a good approximation (figure 4).

Summarizing, a comparison of the intensities of the inner and the outer surface state for $k_{\parallel}$ and $-k_{\parallel}$ mainly provides information on the orbital composition of their wavefunctions. The structure of the intensity, $I = \overline{I} \pm \Delta I$, is similar to those used to describe magnetic linear dichroism [34]. Therefore, one could term the above effect 'linear dichroism in angular distribution'. We note in passing that this dichroism cannot be explained within the free-electron model (see the appendix) and, therefore, can be attributed to the surface symmetry.

5.3. Spin-resolved normal photoemission

As stated in section 4.3, the spin polarization of an initial state and of the related photoelectron may differ, depending on the chosen set-up (i.e., in-plane wavevector $k_{\parallel}$ and energy E). One example where P_N and P_I deviate from each other is that of normal emission ($k_{\parallel} = 0$). Here, the two surface states are degenerate (figure 3) and the net spin polarization P_N vanishes. By excitation with off-normally incident p-polarized light, the photoelectrons excited from the surface states can, however, be spin polarized, with P_I normal to the scattering plane (spanned by the surface normal and the incidence direction of the light) [35, 36]. For light incident within the mirror yz-plane, P_I^x can be the only non-zero P_I component, which in systems with strong SOC can be as large as several tens per cent (e.g., for Pt). A considerable P_I^x could therefore be expected for the Au surface states as well.

It turned out, however, that in the present experiments P_I^x was rather small, i.e., close to the detection limit of about 5% (figure 5(b)). The photoemission calculations could only reproduce these findings when taking into account the real part of the optical potential V_{opt} that was fixed by reproducing the experimental intensity relations (sections 4.2 and 5.2). The theoretical normal-emission spectrum still shows a significant spin polarization (figure 5(a)), but P_I^x is as small as 4.5% (in absolute value) at the peak position. Thus, experiment and theory are consistent with respect to both intensity and photoelectron spin polarization.
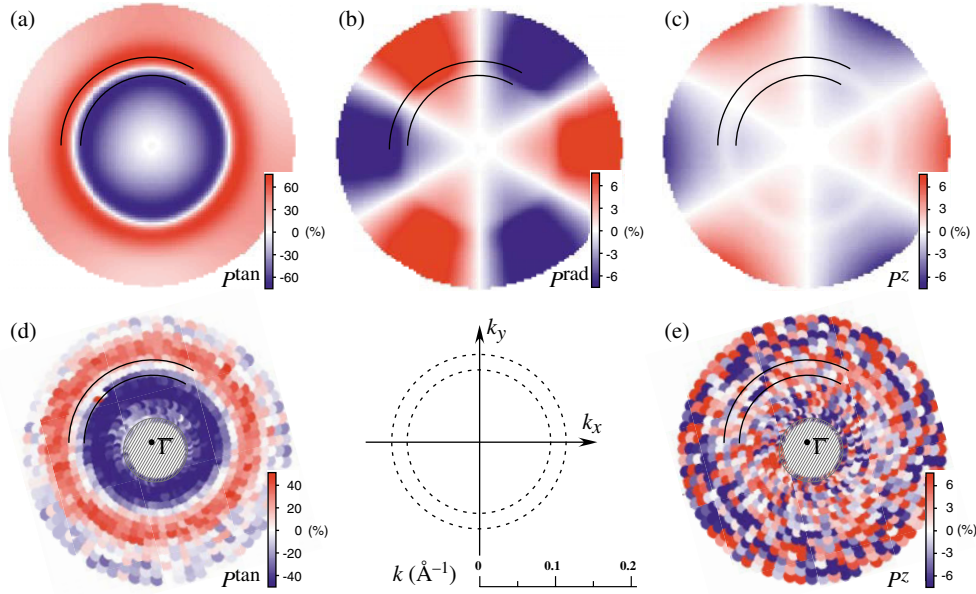
Figure 6. The spin polarization of the photocurrent in the angular distribution at 0.17 eV binding energy. Top row: the calculated polarization maps are decomposed into the tangential component P^{tan} (a), radial component P^{rad} (b) and normal component P^z (c). The peak positions of the inner and outer surface states are indicated by black arcs in a part of the plots. Bottom row: the measured maps for P^{tan} as derived from P^x_{MD} (d) and P^z (e) are shown for comparison. The P^{rad} map was not measured. Note the different colour scales for the various data sets.

5.4. Spin-resolved off-normal photoemission

In order to investigate the spin polarization of the surface states, angle-scanned photoemission calculations and experiments were performed at a fixed binding energy (0.17 eV). The angular distributions of the three components P_I^{tan}, P_I^{rad} and P_I^z of the photoelectron spin polarization $\boldsymbol{P}_I$ are shown in figure 6.

The description of the L-gap surface states in terms of a 2DEG with Rashba–Bychkov SOC suggests reaching a conclusion from the tangential spin polarization P_I^{tan}—measured for both the inner and the outer surface state—as regards the sign of the SOC strength γ (section 2). In both experiment and theory, P_I^{tan} shows a circularly symmetric distribution, with the maximum spin polarization (in absolute value) showing up at the positions of the surface states (indicated by black arcs). Its central part is negative and its outer part is positive (colour coded as blue and red in figures 6(a) and (d)), hence implying that $\gamma > 0$. Since γ is proportional to the z derivative of the crystal potential ($\gamma \propto \partial_z V(z)$; see the appendix) and the maximum spectral weight of the surface states is in the outermost Au layer, the spin–orbit-induced splitting can be attributed to the surface barrier, the potential of which increases from the bulk towards the vacuum.

As was discussed for normal emission (section 5.3), the effect of spin–orbit coupling in the photoemission process itself is rather small in the chosen set-ups. Therefore, $\boldsymbol{P}_N$ and $\boldsymbol{P}_I$ did not differ significantly at $\boldsymbol{k}_\parallel = 0$. For off-normal emission, the theoretical P_I^{tan} is about $\pm 75\%$ at the surface states, which compares rather well with P_N^{tan} for the inner and the outer surface state (-97% and 93% for α). This agreement shows up also in P^z, for which the

tiny P_I^z is consistent with β values of 1.4% and -1.3% for the inner and the outer surface state (compare (4)). The experimental counterparts for P^{tan} and P^z are shown in figures 6(d) and (e). For the tangential component one finds a nice agreement with theory considering the ring structure of the spin polarization. The maximum values of P^{tan} are about 2/3 of those in theory due to the strong overlap of the peaks that appear broadened by the relaxed resolution and due to the contribution of an unpolarized background in the spectra (these effects are not included in the theoretical calculations). The observed degrees of polarization are consistent with the instrumental resolution. Summarizing, for off-normal emission one can also reach a conclusion—at least semi-quantitatively—from the spin polarization of the photoelectrons on that of the surface states.

Both the analytical theory (section 2) and the first-principles calculations allow for a modulation of the spin polarization $\boldsymbol{P}_N$ with azimuth φ_e due to the threefold symmetry of the Au(111) surface, which should lead to a modulation in $\boldsymbol{P}_I$. Symmetry dictates that for emission within a mirror plane of the surface the radial component P^{rad} vanishes (only $P^{\text{tan}} \neq 0$ is permitted). This is clearly visible in the $\overline{\Gamma}$–$\overline{\text{K}}$ azimuth ($k_x = 0$) and its two equivalents, the latter being rotated about $\pm 60°$. The mirror symmetry implies further that $P^{\text{rad}}(90° - \varphi_e) = -P^{\text{rad}}(90° + \varphi_e)$, which turns positive into negative polarization and vice versa, under reflection at the k_y-axis (centre of figure 6(b)). Note that the magnitude of P_I^{rad} becomes almost zero at the radii of the surface states, indicating a very small threefold modulation with the azimuth (point group C_3). For the normal component P_I^z (figure 6(c)) the same symmetry considerations as for P^{rad} hold. Compared to the P_I^{rad} case, two rings of almost zero spin polarization at the radii of the surface states can be clearly observed. There is apparently no significant threefold modulation in P_I^{tan} for both experiment and theory.

Former photoemission calculations showed a threefold modulation of the spin polarization [14] which was considerably larger than that presented here. The improved agreement between theory and experiment results from fine-tuning the free parameters in photoemission theory, in particular the real part of the optical potential. The latter could be calculated from first principles within the GW approximation [37]. Therefore, the Au(111) surface lends support to so demanding an investigation.

Focusing on the experimental P^z (figure 6(e)), one finds no significant structure in the angular distribution within the noise. Taking into account the detection limit of about 5%, this finding is consistent with the theoretical results (figure 6(c)) because in the latter the spin polarization is less than this limit (in absolute value).

In summary, for the chosen set-up (p-polarized light with 21.1 eV photon energy) the photoelectron spin polarization $\boldsymbol{P}_I$ is tangentially aligned and no significant threefold modulation shows up (within the detection limit). Hence, it is fully consistent with the spin polarization $\boldsymbol{P}_N$ of the initial surface states, except as regards its degree. The latter is about ± 96%, as obtained from first-principles calculations, considerably larger than that in the photoemission (about ± 45% in experiment and ± 75% in theory).

5.5. Effects of spin–orbit coupling and surface corrugation

The effect of spin–orbit coupling on the spin polarization of the surface states is addressed theoretically. The different behaviours of inner and outer surface states can be elucidated by scaling the SOC strength x in the Dirac Hamiltonian of the *ab initio* calculations (compare section 4.1). In the scalar-relativistic case ($x = 0$ in figure 7(a)), the splitting of the L-gap surface states vanishes, leading to $P_N^{\text{tan}} = 0$ (figure 7(b)). The splitting increases with x, leaving the position (along the k_y-axis) of the inner state almost unaffected, while the outer is shifted to larger k_y. For $x = 0.5$, both states almost maintain their pure spin up and spin
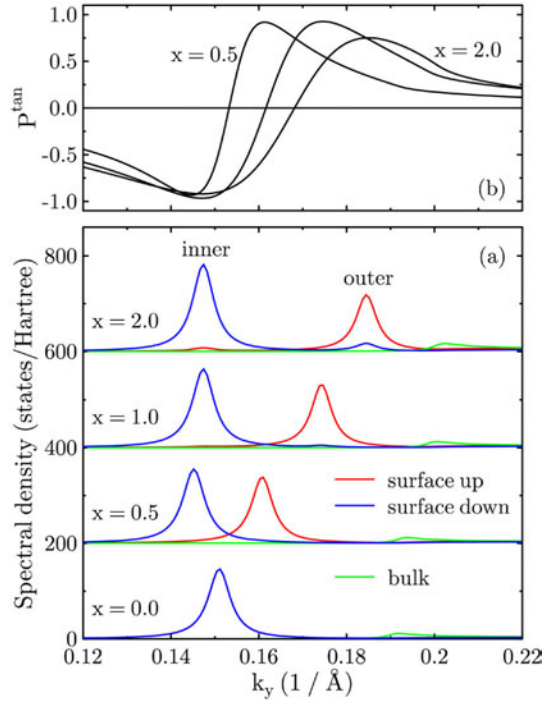
Figure 7. The effect of spin–orbit coupling on the L-gap surface states. (a) Spin-resolved spectral densities of the surface states (solid and dashed (blue and red)) at the outermost Au layer and of a bulk layer (dotted (green)) for SOC scaled from $x = 0$ (scalar-relativistic) via $x = 1$ (fully relativistic) to $x = 2.0$ ('super-relativistic'), as indicated on the left. The wavevector is along $\overline{\Gamma}$–$\overline{M}$ (along the k_y-axis); the energy is E_F. The offset between adjacent spectra is 200 states Hartree^{-1}. 'Surface up' and 'surface down' refer to $P_N^{\tan} > 0$ and $P_N^{\tan} < 0$, respectively. (b) The tangential spin polarization $P_N^{\tan}$ of the L-gap surface states obtained from the data presented in (a).

down character, while for $x = 1$ (fully relativistic case) contributions to the spectral density of the other spin orientation become mixed in. This is particularly evident for the outer surface state where a significant spin down maximum (dashed (blue) in figure 7(a)) shows up. For the inner surface state, the admixture is considerably less. In the 'super-relativistic' case ($x = 2.0$) these opposite-spin contributions become even more pronounced, further reducing the spin polarization (in absolute value) as compared to the case $x = 1$ (figure 7(b)).

A reason for this difference between the inner and the outer surface state can be seen in spin-dependent scattering at bulk states (green in figure 7(a)). Because the outer surface state is closer in reciprocal space to the bulk states than the inner one, it might be more affected by spin–orbit-induced spin-flip scattering, as is corroborated from $P_N^{\tan}$ (figure 7(b)). Note in this context that the two surface states are not strongly localized at the surface but show considerable spectral weight in the first ten surface layers [6, 14]. Further, the k_y distance between the outer surface state and the bulk states decreases with increasing x. Accompanied with the reduction of the spin polarization of the outer surface state, compared to that of the inner, is an increased modulation of P with φ_e, as is evident from figures 6(a)–(c). This finding is consistent with the smaller degree of modulation in the experimental momentum distribution: the experimental k distance between the outer surface state and the bulk states of 0.044 Å^{-1} (compare figure 2 in [6]) is larger than in theory (0.026 Å^{-1} for $x = 1$). To summarize, the different locations of the surface states in reciprocal space manifest themselves in deviations

from the 2DEG behaviour. The inner surface state behaves more like a free-electron state; the outer is slightly more influenced by bulk states. In order to test the proposed explanation, one could investigate the spin polarization of the surface states on different vicinal Au(111) surfaces, thereby changing the k distance to the bulk states.

In order to test the effect of corrugation on the spin polarization of the L-gap surface states, the surface barrier built with the muffin-tin potentials was replaced by a smooth *uncorrugated* barrier shape [32]. The parameters of the latter were obtained by fitting the dispersions of the L-gap surface states to those for the *corrugated* muffin-tin barrier. Since dispersions and binding energies agreed very well for the two surface barriers, one could switch the surface corrugation on and off without affecting relevant parts of the electronic structure. The corrugation manifests itself particularly in a non-zero P_N^z (section 2). At the Fermi energy for $k_\parallel$ along $\overline{\Gamma}$–$\overline{K}$, one obtains from the spectral density for the corrugated surface +1.45% for the inner and −1.32% for the outer surface state. For the uncorrugated surface, P_N^z is slightly reduced (in absolute value) to +0.99% and −0.88%, respectively. This humble change in P_N^z is explained by the considerable extension of the surface-state wavefunction within the ten outermost surface layers. Hence, only a small part of it is affected by the surface barrier potential, which, however, is sufficiently large to produce an observable spin–orbit splitting.

6. Concluding remarks

The present joint investigation on the L-gap surface states on Au(111) provides details of their anatomy. The spin- and angle-resolved photoemission experiments agree qualitatively and semi-quantitatively with first-principles calculations, being directly linked by numerical photoemission calculations.

One could think of several extensions of the present work. First, one could deal with a modification of the electronic structure at vicinal Au(111) surfaces. The surface states would propagate freely along the terraces but could be confined to directions perpendicular to the steps. Thus, the two-dimensional surface states become one-dimensional [38, 39]. The step-induced umklapp processes would lower the binding energy and would also lead to smaller lifetimes due to increased scattering at bulk states. As was evidenced in section 5.5, this could have a pronounced effect on both degree and direction of the surface-state spin polarization. Second, one could investigate the modification of the surface states upon adding magnetic atoms onto Au(111). Here, the electronic structure of the 2DEG is subject to spin-dependent scattering at the magnetic impurities. And lastly, one could compute the self-energy within the GW approximation, in order to compare it with the optical potential deduced here from the comparison of experimental with theoretical photoemission spectra (section 4.2).

Acknowledgments

Appendix. Two-dimensional electron gas with Rashba–Bychkov spin–orbit interaction

The non-relativistic Hamilton operator for electrons with spin–orbit interaction is given by [40, 41]

$$H = \frac{1}{2}p^2 + V(r) + \frac{1}{2c^2}\sigma \cdot [\nabla V(r) \times p], \tag{A.1}$$

with $\boldsymbol{\sigma}$ the vector of Pauli matrices and $\boldsymbol{p} = -i\boldsymbol{\nabla}$ the momentum operator (in Hartree atomic units, $e = m = \hbar = 1$, $c \approx 137$). In order to form a two-dimensional electron gas (2DEG), the potential V has to confine the electrons to a plane (say $z = 0$) and allow for free motion within that plane (i.e., $V = V(z)$). Assuming without loss of generality $V(0) = 0$, the Hamiltonian for the 2DEG then reads

$$H = -\frac{1}{2}(\partial_x^2 + \partial_y^2) + i\frac{\partial_z V(z)|_{z=0}}{2c^2}\left(\sigma_x \partial_y - \sigma_y \partial_x\right). \tag{A.2}$$

The ansatz $\psi_{\boldsymbol{k}}$ for the eigenfunctions consists of a plane-wave spinor,

$$\psi_{\boldsymbol{k}}(\boldsymbol{r}) = (\mu_{\boldsymbol{k}}\chi^+ + \nu_{\boldsymbol{k}}\chi^-)e^{i(k_x x + k_y y)}, \tag{A.3}$$

with $\boldsymbol{k} = (k_x, k_y)$ and $\boldsymbol{r} = (x, y)$. The Pauli spinors $\chi^{\pm}$ are quantized with respect to the z-axis ($\sigma_z \chi^{\pm} = \pm\chi^{\pm}$). With $\sigma_x \chi^{\pm} = \chi^{\mp}$ and $\sigma_y \chi^{\pm} = \pm i\chi^{\mp}$, the Schrödinger equation $H\psi_{\boldsymbol{k}} = E(\boldsymbol{k})\psi_{\boldsymbol{k}}$ yields the condition

$$(k_y + ik_x)\nu_{\boldsymbol{k}}^2 = (k_y - ik_x)\mu_{\boldsymbol{k}}^2 \tag{A.4}$$

for the coefficients $\mu_{\boldsymbol{k}}$ and $\nu_{\boldsymbol{k}}$. Normalization of $\psi_{\boldsymbol{k}}$ results in two sets of coefficients (indexed by $\pm$),

$$\mu_{\boldsymbol{k}\pm} = \frac{1}{\sqrt{2}}, \qquad \nu_{\boldsymbol{k}\pm} = \mp\frac{1}{\sqrt{2}}\sqrt{\frac{k_y - ik_x}{k_y + ik_x}} \qquad \text{for } k \neq 0. \tag{A.5}$$

The eigenvalues of $\psi_{\boldsymbol{k}\pm}$ are given by

$$E_{\pm}(\boldsymbol{k}) = \tfrac{1}{2}k^2 \pm \gamma|\boldsymbol{k}|, \tag{A.6}$$

with $\gamma = \partial_z V(z)|_{z=0}/(2c^2)$. Hence, the strength of the spin–orbit-induced splitting, $E_+(\boldsymbol{k}) - E_-(\boldsymbol{k}) = 2\gamma$, is proportional to the structural asymmetry given by $\partial_z V$. The spin polarization $\boldsymbol{P}_{\pm}(\boldsymbol{k}) = \psi_{\boldsymbol{k}\pm}^{\dagger}\boldsymbol{\sigma}\psi_{\boldsymbol{k}\pm}$ is complete and perpendicular to $\boldsymbol{k}$,

$$P_{\pm}^x(\boldsymbol{k}) = \mp\frac{k_y}{|\boldsymbol{k}|}, \qquad P_{\pm}^y(\boldsymbol{k}) = \pm\frac{k_x}{|\boldsymbol{k}|}, \qquad P_{\pm}^z(\boldsymbol{k}) = 0. \tag{A.7}$$

Hence, $\boldsymbol{P}_+$ ($\boldsymbol{P}_-$) rotates anticlockwise (clockwise) around the z-axis.

Note that the sign of γ determines the order of the spin–orbit-split states in reciprocal space, that is, which one is the inner and which one is the outer in the momentum distribution. But since it does not affect the spin polarization, the latter—for instance obtained from experiment—is a measure for the sign of γ.

References

[1] Rashba E I 1960 *Sov. Phys.—Solid State* **2** 1109
[2] Bychkov Y A and Rashba E I 1984 *Sov. Phys.—JETP Lett.* **39** 78
[3] LaShell S, McDougall B A and Jensen E 1996 *Phys. Rev. Lett.* **77** 3419
[4] Reinert F 2003 *J. Phys.: Condens. Matter* **15** S693
[5] Reinert F, Nicolay G, Schmidt S, Ehm D and Hüfner S 2001 *Phys. Rev.* B **63** 115415
[6] Nicolay G, Reinert F, Hüfner S and Blaha P 2001 *Phys. Rev.* B **65** 033407
[7] Petersen L and Hedegård P 2000 *Surf. Sci.* **459** 49
[8] Muntwiler M, Hoesch M, Petrov V N, Hengsberger M, Patthey L, Shi M, Falub M, Greber T and Osterwalder J 2004 *J. Electron Spectrosc. Relat. Phenom.* **137** 119
[9] Hoesch M, Muntwiler M, Petrov V N, Hengsberger M, Patthey L, Shi M, Falub M, Greber T and Osterwalder J 2004 *Phys. Rev.* B **69** 241401
[10] Bürgi L, Petersen L, Brune H and Kern K 2000 *Surf. Sci.* **447** L157
[11] Henk J, Ernst A and Bruno P 2003 Spin polarization of the L-gap surface states on Au(111) *Preprint* cond-mat/0305530

[12] Hoesch M, Greber T, Petrov V N, Muntwiler M, Hengsberger M, Auwärter W and Osterwalder J 2002 *J. Electron Spectrosc. Relat. Phenom.* **124** 263

[13] Feder R and Henk J 1996 *Spin–Orbit Influenced Spectroscopies of Magnetic Solids* (*Springer Lecture Notes in Physics* vol 466) ed H Ebert and G Schütz (Berlin: Springer) p 85

[14] Henk J, Ernst A and Bruno P 2003 *Phys. Rev.* B **68** 165416

[15] Dresselhaus G 1955 *Phys. Rev.* **100** 580

[16] Mugarza A, Mascaraque A, Repain V, Rousset S, Altmann K N, Himpsel F J, Koroteev Y M, Chulkov E V, García de Abajo F J and Ortega J E 2002 *Phys. Rev.* B **66** 245419

[17] Perdew J P and Wang Y 1992 *Phys. Rev.* B **45** 13244

[18] Hüfner S 2003 *Photoelectron Spectroscopy* 3rd edn (Berlin: Springer)

[19] Fujita D, Amemya K, Yakabe T, Nejoh H, Sato T and Iwatsuki M 1999 *Surf. Sci.* **423** 160

[20] Crljen Ž, Lasić P, Šokčević D and Brako R 2003 *Phys. Rev.* B **68** 195411

[21] Reinert F and Nicolay G 2004 *Appl. Phys.* A **78** 817

[22] Tamura E 1996 private communication

[23] Ebert H, Freyer H and Deng M 1997 *Phys. Rev.* B **56** 9454

[24] Taut M, Ernst A and Eschrig H 1998 *J. Phys. B: At. Mol. Opt. Phys.* **31** 2689

[25] Braun J 1996 *Rep. Prog. Phys.* **59** 1267

[26] Henk J 2001 *Handbook of Thin Film Materials* vol 2, ed H S Nalwa (San Diego, CA: Academic) chapter 10, p 479

[27] Hedin L 1999 *J. Phys.: Condens. Matter* **11** R489

[28] Rampe A, Güntherodt G, Hartmann D, Henk J, Scheunemann T and Feder R 1998 *Phys. Rev.* B **57** 14370

[29] Scheunemann T 1993 Zur Theorie der Photoemission: Elektromagnetisches Feld an Metalloberflächen im hydrodynamischen Modell *Diploma Thesis* Universität Duisburg Theoretische Festkörperphysik

[30] Mazin I I 1999 *Phys. Rev. Lett.* **83** 1427

[31] Jonker B T, Hanbicki A T, Pierce D T and Stiles M D 2004 *J. Magn. Magn. Mater.* **277** 24

[32] Henk J, Schattke W, Carstensen H, Manzke R and Skibowski M 1993 *Phys. Rev.* B **47** 2251

[33] Inui T, Tanabe Y and Onodera Y 1990 *Group Theory and its Applications in Physics* (*Springer Series in Solid State Sciences* vol 78) (Berlin: Springer)

[34] Henk J, Scheunemann T, Halilov S V and Feder R 1996 *J. Phys.: Condens. Matter* **8** 47

[35] Tamura E, Piepke W and Feder R 1987 *Phys. Rev. Lett.* **59** 934

[36] Tamura E and Feder R 1991 *Europhys. Lett.* **16** 695

[37] Aryasetiawan F and Gunnarson O 1998 *Rep. Prog. Phys.* **61** 237

[38] Mugarza A, Mascaraque A, Pérez-Dieste V, Repain V, Rousset S, García de Abajo F J and Ortega J E 2001 *Phys. Rev. Lett.* **87** 107601

[39] Ortega J E, Mugarza A, Repain V, Rousset S, Pérez-Dieste V and Mascaraque A 2002 *Phys. Rev.* B **65** 165413

[40] Rose E M 1961 *Relativistic Electron Theory* (New York: Wiley)

[41] Kessler J 1985 *Polarized Electrons* (*Springer Series on Atoms and Plasmas* vol 1) 2nd edn (Berlin: Springer)